IEEE Access
Multidisciplinary | Rapid Review | Open Access Journal

Received 7 October 2025, accepted 24 November 2025, date of publication 27 November 2025,
date of current version 4 December 2025.

Digital Object Identifier 10.1109/ACCESS.2025.3638278

RESEARCH ARTICLE

A Practical Thermal Model for Temperature Estimation in Outer-Rotor Permanent-Magnet Synchronous Motors

IRVING S. AGUILAR-ZAMORATE[1], RENATO GALLUZZI[1], (Senior Member, IEEE), SAULIUS PAKŠTYS[2], ERICK AXEL MARTINEZ-RÍOS[1], AND NICOLA AMATI[2]

[1]School of Engineering and Sciences, Tecnologico de Monterrey, Mexico City 14380, Mexico
[2]Center for Automotive Research and Sustainable Mobility, Politecnico di Torino, 10129 Turin, Italy

Corresponding author: Renato Galluzzi (renato.galluzzi@tec.mx)

This work was supported in part by the EM-TECH Research Project part of 2Zero funded by European Commission under Grant 101096083. The work of Irving S. Aguilar-Zamorate and Erick Axel Martinez-Ríos was supported by the Secretaría de Ciencia, Humanidades, Tecnología e Innovación (SECIHTI) under Grant 1010770 and Grant 1105077. The work of Saulius Pakštys was supported by the PNRR-NGEU Project from MUR under Grant DM 352/2022.

ABSTRACT Temperature monitoring of rotating electric machines is necessary to ensure proper and safe operation. In many difficult-to-access locations, such as the rotor, direct measurements are difficult to implement due to complexity and cost limitations. Estimation methods are a valid alternative and, among the possibilities, low-order lumped-parameter thermal networks offer simplicity and computational affordability for their implementation in real time. However, a critical factor influencing the performance of these models is the accurate estimation of the initial state. This paper develops and validates a two-node thermal network that uses winding temperature feedback to estimate the rotor temperature in an outer-rotor permanent-magnet synchronous machine. The proposed method is validated using a comprehensive experimental dataset collection, including a standardized driving cycle across diverse coolant temperatures and flow rates. It is demonstrated that the proposed solution achieves a root-mean-squared temperature error of 1.09°C in average across the validation duty cycles.

INDEX TERMS Lumped-parameter thermal networks, low-order models, temperature estimation, permanent-magnet synchronous motors.

I. INTRODUCTION

Permanent-magnet synchronous machines (PMSMs) are used in a wide range of applications. In electric mobility solutions, they are favored due to their advantageous power and torque densities, efficiency and reliability [1]. Nonetheless, demanding duty cycles, which are evident in vehicle traction applications, can lead to an irreversible demagnetization of the rotor permanent magnets due to overheating [2]. High temperatures may damage the quality of the winding insulation. Since thermal incidences can potentially degrade performance, temperature monitoring is key for guaranteeing the integrity of the motor. For these reasons, thermal diagnosis methods represent a research area that has garnered significant interest from both industry and academia [3].

PMSMs in electric vehicles typically incorporate thermistors (e.g., PT100) as temperature sensors embedded in the winding hotspots [4]. They are used to prevent faults due to insulation melting and accelerated aging from excessive thermal loads [5]. However, the direct monitoring of the magnet temperature is more critical due to the issues associated with rotational motion, especially at high speeds [6]. Direct contact methods require additional elements for signal transmission, such as slip rings and brushes or wireless transmitters/receivers. These additional subsystems significantly increase the complexity of the machine [7]. Moreover, the minimal space in the air gap and the magnet

The associate editor coordinating the review of this manuscript and approving it for publication was Qinfen Lu.

slots hinders the placement of physical sensors. Alternatively, contactless measurements using infrared sensors [8] or thermal imaging cameras are cost-prohibitive for the vast majority of applications in the industry. These solutions require the visibility of the magnets, which may not be viable for all applications [9].

With this background, an extensive set of temperature estimation methods has been proposed in the literature in recent years. These approaches can be categorized as model-based, physics-informed, and data-driven [4]. Model-based methods include computational fluid dynamics and finite element analysis [10]. Although these calculations can be refined to attain high precision, they are not suitable for real-time applications due to their calculation time and computational effort. Electrical model-based methods are centered on observing a temperature-related electrical parameter by direct or indirect means. The former can be based on injecting a high-frequency signal carrier to estimate the stator impedance, which can be correlated to the magnet temperature [11]. This technique increases the power losses significantly, and its measurements are strongly sensitive to noise. Flux observers are an example of an indirect method exploiting the linear relationship between magnet flux and magnet temperature [12]. However, since the magnet flux depends on the back-electromotive force of the machine, low-speed performance becomes poor in terms of signal-to-noise ratio [13].

Physics-based methods are those centered on mathematical representations of physical phenomena, offering the key advantage of interpretability [4]. The lumped-parameter thermal network (LPTN) is one such method, where heat transfer dynamics are represented as a set of ordinary differential equations governing an equivalent electrical circuit. LPTNs can be classified according to model order, i.e., the number of thermal nodes or states in the system. They can be categorized into (i) dark gray-box LPTN (with two to four nodes), (ii) light gray-box LPTN (with five to fourteen nodes), and (iii) white-box LPTN (with fifteen nodes or more) [14]. Low-order models have gained attention for real-time applications due to their simplicity, which facilitates their implementation and deployment on low-cost microcontrollers. Moreover, parameter identification can be performed using experimental measurements to fit the model parameters without requiring considerable information about the machine's properties [15].

Data-driven approaches have also been explored in the literature, with solutions including Long Short-term Memory (LSTM) networks [16], [17], combinations of diverse neural networks (NNs), such as recurrent and convolutional NNs (RNNs and CNNs, respectively) [18] and feed-forward NNs (FFNN) [19], and supervised machine learning (ML) methods [20]. Although these methods can provide an accurate temperature estimation and no machine parameters are required to be known a priori, they need large datasets that cover the entire operating range of the machine for proper tuning or training [9]. Additionally, they have significantly more parameters than reduced-order LPTNs, making their real-time implementation almost impractical in low-cost and real-time hardware [21].

The work herein proposes and analyzes a second-order lumped-parameter thermal network to estimate the rotor temperature of an outer-rotor radial-flux PMSM for automotive powertrains. This method guarantees affordability from the computational standpoint, while still providing acceptable temperature estimates. In particular, to enhance accuracy, temperature feedback from the machine's winding is included as an input to the LPTN. Unlike flux observers, which infer the magnet temperature indirectly from variations in magnetic flux and are highly sensitive to parameter uncertainties, a dedicated sensor embedded in the windings offers a direct measurement of the temperature changes within the machine [22]. Additionally, a method for properly setting the initial conditions of the LPTN is proposed. The presented approach is validated through a complete dataset collection, including stationary working points and a standardized driving cycle, where the behavior of the cooling circuit is varied intentionally to study the heat transfer features of the machine under study. Finally, the real-time deployment feasibility of the proposed method is tested on a Texas Instruments TMS320F28069M microcontroller.

II. METHOD

The present method is based on the use of a low-order LPTN to reproduce the temperature behavior of a powertrain machine. An LPTN is generally formed by four key element types: temperature sources, thermal capacitances, power losses, and thermal resistances. In the electrical domain, these are equivalent to the voltage sources, electrical capacitances, current sources, and electrical resistances, respectively [14].

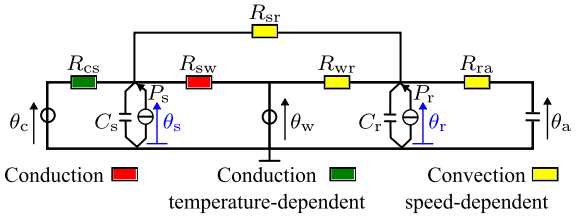

FIGURE 1. Second order lumped-parameter thermal network (LPTN) with winding temperature feedback. Estimated temperatures are marked in blue.

The LPTN shown in Fig. 1 is based on the low-order model for PMSMs proposed by Wallscheid and Bocker [14]. This system solves for the temperatures of the stator (θ_s) and the rotor (θ_r). These variables constitute the states of the system, while the temperatures of the coolant (θ_c), winding (θ_w) and ambient (θ_a) are known measurements. From a practical perspective, these latter variables are available from dedicated sensors that can be easily installed. This is not the case for the rotor, where the positioning of a measurement device is complex and costly.

Terms C_s and C_r denote the thermal capacitances of the stator and rotor bodies, respectively. Due to the speed

convection and coolant temperature-dependent resistances present in the network, the LPTN is a linear parameter-varying model. Therefore, the thermal resistances are classified into convection resistances (R_{wr}, R_{sr}, R_{ra}), and conduction resistances (R_{cs}, R_{sw}). R_{sw} is a fixed conduction resistance, while R_{cs} is a coolant temperature-dependent resistance modeled using

$$R_{cs} = R_{cs0}\left[1 + \alpha_{cs}(\theta_c - \theta_{c0})\right] \tag{1}$$

$$\alpha_{cs} \in \{\mathbb{R} \mid -1\%/\mathrm{K} \leq \alpha_{cs} \leq 0\} \tag{2}$$

where θ_{c0} is the nominal coolant temperature (40° C). The speed-dependent convection resistances are modeled using the equations introduced in [23] and [24]:

$$R_{ij}(n) = R_{ij0} \exp\left(-\frac{\omega}{\omega_{max}} \frac{1}{b_{ij}}\right) + a_{ij} \tag{3}$$

with

$$R_{ij0} \in \left\{\mathbb{R} \mid 0 \leq R_{ij0} \leq R_{ij0,max}\right\}$$
$$b_{ij} \in \left\{\mathbb{R} \mid 0 \leq b_{ij0} \leq b_{ij0,max}\right\}$$
$$a_{ij} \in \left\{\mathbb{R} \mid 0 \leq a_{ij0} \leq a_{ij0,max}\right\}$$

where R_{ij0}, b_{ij}, and a_{ij} are constants to be fitted, while ω is the motor speed. Thus, the resistance can be split into a constant and exponential terms, the latter being dependent on ω.

Power losses in the stator yoke, rotor yoke, and magnets are derived from finite-element computations using Ansys Motor-CAD and stored into dedicated look-up tables. Specifically, iron losses in the stator and rotor laminations are governed by the Bertotti model [25], characterized by hysteresis, eddy currents, and excess loss components. Magnet Joule losses due to eddy currents are also computed [26]. In the LPTN node, the rotor power source P_r groups the rotor yoke losses (P_{ry}) and magnet losses (P_{pm}):

$$P_r = P_{ry} + P_{pm} \tag{4}$$

Fig. 2 shows the normalized total electric losses in the torque-speed plane used in the model. They are the summation of the stator and rotor components:

$$P = P_s + P_r \tag{5}$$

The heat transfer in each node of the LPTN can be represented as an ordinary differential equation given by [3]

$$C_i \frac{\mathrm{d}\theta_i(t)}{\mathrm{d}t} = \sum_{\substack{j=1 \\ j\neq i}} \frac{\theta_j(t) - \theta_i(t)}{R_{ij}} + \sum_{k=1}^{m} \frac{\theta_{ex,k}(t) - \theta_i(t)}{R_{ik}} + P_i(t) \tag{6}$$

where $i = 1 \ldots n$ are the LPTN nodes containing the thermal capacitances C_i and the power sources P_i, while $k = 1 \ldots m$ are the boundary nodes represented by the temperature exogenous sources θ_{ex}. The resulting equations can be expressed in state-space form:

$$\dot{\mathbf{x}} = \mathbf{A}\mathbf{x} + \mathbf{B}\mathbf{u} \tag{7}$$

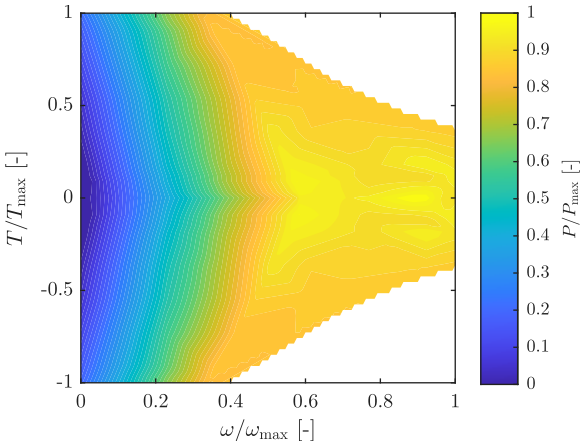

FIGURE 2. Total electric losses in the rotor and stator power nodes plotted in the torque-speed plane.

$$\mathbf{y} = \mathbf{C}\mathbf{x} + \mathbf{D}\mathbf{u} \tag{8}$$

where

$$\mathbf{A} = \begin{bmatrix} -\dfrac{G_{sw} + G_{sr} + G_{cs}}{C_y} & \dfrac{G_{sr}}{C_y} \\ \dfrac{G_{sr}}{C_m} & -\dfrac{G_{ra} + G_{wr} + G_{yr}}{C_m} \end{bmatrix}$$

$$\mathbf{B} = \begin{bmatrix} C_s^{-1} & 0 & C_s^{-1}G_{sw} & C_s^{-1}G_{cs} & 0 \\ 0 & C_r^{-1} & C_r^{-1}G_{wr} & 0 & C_r^{-1}G_{ra} \end{bmatrix}$$

$$\mathbf{C} = \mathbf{I}_{2\times 2}, \quad \mathbf{D} = \mathbf{0}_{2\times 5}$$

$$\mathbf{x} = \begin{bmatrix}\theta_s & \theta_r\end{bmatrix}^\top, \quad \mathbf{u} = \begin{bmatrix}P_s & P_r & \theta_w & \theta_c & \theta_a\end{bmatrix}^\top$$

The term G_{ij} is the thermal conductance which is the inverse of the thermal resistance between nodes i and j.

Due to the linear time-variant behavior, the LPTN is discretized using the explicit Euler method using a first-order approximation:

$$\hat{\Phi} = \mathbf{I} + T_s\mathbf{A} \tag{9}$$

$$\mathbf{H} = T_s\mathbf{B} \tag{10}$$

where $\mathbf{I}$ is the identity matrix and T_s is the sampling time. As indicated by [27], the model is numerically stable if the eigenvalues s_i of the continuous-time system fulfill the following inequality:

$$s_i + \frac{1}{T_s} < \frac{1}{T_s} \tag{11}$$

A. EXPERIMENTAL DATA

A comprehensive dataset collection was produced for tuning and validation purposes which is listed in Table 1. The testbed setup consists of two 200-kW in-wheel electric machines mounted in a back-to-back configuration. Both machines are identical outer-rotor radial-flux surface-mounted PMSMs: one is the tested prototype, while the other is the load machine. Machines have 180 slots and 60 magnet poles, with an outer diameter of 456 mm and a stack length of 73 mm. They can reach a maximum torque of 1.65 kNm and

a maximum speed of 1.3 kr/min. The cooling system consists of a cooling jacket circulating a liquid coolant. A note is that this test configuration was previously used in [22], however, the dataset is entirely different as described subsequently.

The tuning dataset is based on nine tests which can be grouped into three categories. The first category, labeled WLTP, is illustrated in Fig. 3. It consists of a pre-heating period followed by the Worldwide Harmonized Light Vehicles Test Procedure (WLTP) type 3 driving cycle. This speed profile was prepared to satisfy the demand of an electric powertrain for an A-class vehicle. Additionally, it was included as a more realistic scenario for the temperature estimation compared with most of the efforts in the literature, which consider steady-state working points almost exclusively. The second category, named LS, consists of two preheating periods, as seen in Fig. 4: one at low speed (50 r/min) and another at medium speed (600 r/min). These two conditions were selected to fit the speed-dependent convection resistances in a sufficiently wide speed range. These first two driving cycle categories were conducted at inlet coolant temperatures of 0° C, 20° C, 40° C and 60° C. It is worth noting that the flow rate was controlled using a manual valve. Thus, it varied during the tests due to temperature-induced changes in the fluid's density and viscosity. The third category is a continuous working point C1 at 370 r/min and 600 Nm. This condition, selected because of its high coolant flow rate (14.8 l/min), sets a sufficiently large upper bound for parameter fitting purposes.

The validation dataset consists of five tests. The first is denoted as a pulse-hold cycle (PH), a set of continuous working points that covers all the speed operating range of the machine (see Fig. 5). Subsequently, two mixed driving cycles are applied with preheating and the WLTP (see Fig. 3). Both cycles apply coolant flow rates of 10.7 l/min (WLTP-FR1) and 14.9 l/min (WLTP-FR2), respectively, while the inlet coolant temperature is set to 20° C. Finally, two steady-state working points (C1, C2) are evaluated. The latter requests a slightly larger torque of 700 Nm with respect to C1 at the same angular speed.

Table 1 summarizes the features of all the duty cycles aimed at the tuning and validation steps.

TABLE 1. Tuning (T) and Validation (V) duty cycles parameters.

Test	Key	Type	θ_{in} [°C]	Flow rate [l/min]	θ_{a} [°C]
1	WLTP-0	T	0	13.4	21
2	LS-0	T	0	13.4	21
3	WLTP-20	T	20	10.7	21
4	LS-20	T	20	10.7	21
5	WLTP-40	T	40	10.6	21
6	LS-40	T	40	10.5	21
7	WLTP-60	T	60	10.6	24
8	LS-60	T	60	10.6	24
9	C1-60	T	60	14.8	21
10	PH-20	V	20	10.7	21
11	WLTP-FR1	V	20	10.7	21
12	C1-30	V	30	14.9	21
13	C2-40	V	40	15.0	21
14	WLTP-FR2	V	20	14.9	21

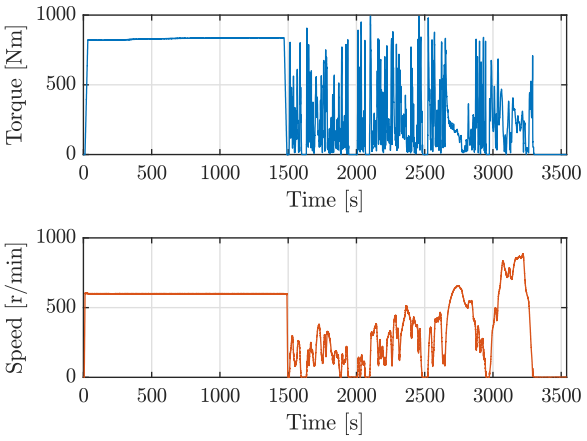

FIGURE 3. Driving cycle displaying preheating and WLTP portions. Motor torque (top) and angular speed (bottom).

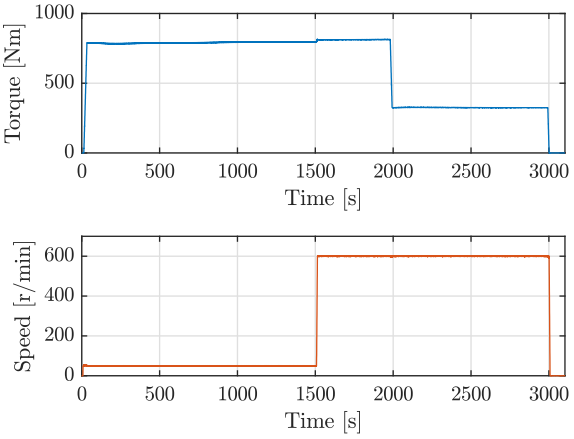

FIGURE 4. Driving cycle for low and medium speeds. Motor torque (top) and angular speed (bottom).

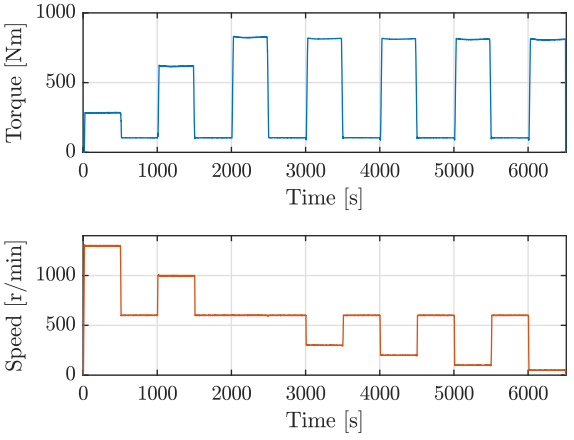

FIGURE 5. Pulse hold driving cycle. Motor torque (top) and angular speed (bottom).

In the experimental setup illustrated in Fig. 6, the dyno load imposes its angular speed to the unit under test, which in turn is torque-controlled. The winding temperature is measured in its end-turn hotspot using a glass-encapsulated

thermistor (TDK EPCOS B57551G1103). The thermistor has a resistivity tolerance of ±2% or ±0.4° C that covers the range within −10 and 300° C. Two additional thermistors of the same type are used to monitor coolant temperature at the inlet and outlet of the circuit. The input coolant temperature for the model θ_c is the average between the inlet θ_{in} and outlet θ_{out} temperatures. Additionally, the ambient temperature θ_a is equalized to a constant, measured room temperature.

The rotor surface temperature is registered using an infrared sensor Calex PyroCouple PC151MT-0 characterized by a fixed emissivity (0.95) within the operating range from 0 to 250° C. The sensor has a repeatability of ±0.5% or ±0.5° C, and an accuracy of ±1% or ±1° C, whichever is larger from both values. The inclusion of this sensor allows for the validation of the low-order LPTN model, as the rotor temperature is the most relevant state of interest.

A National Instruments cDAQ 9184 chassis equipped with a 9205 16-bit analog input module was used to acquired the temperature data. The torque was registered using a Kistler 4503A2K0L00B1000 torque transducer that has an accuracy of ±1 Nm. It was located in a series configuration between the rotor of the two machines and includes a built-in speed transducer. The data was captured using a sampling frequency of 5 Hz which guarantees covering the main thermal and mechanical dynamics with enough temporal resolution.

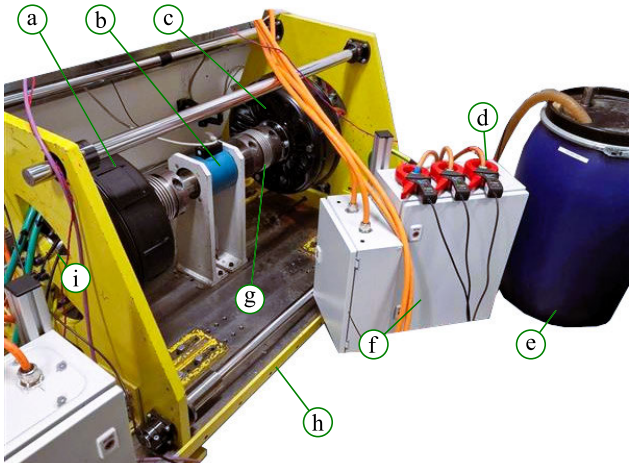

FIGURE 6. Back-to-back motor testbed to produce the datasets for tuning and validation of the LPTN model. ⓐ Dyno load motor, ⓑ torque meter, ⓒ motor under test, ⓓ current proble (×3), ⓔ coolant reservoir, ⓕ three-phase inverter (×2), ⓖ flexible coupling (×2), ⓗ frame, ⓘ phase connections and cooling pipes.

B. LPTN PARAMETER TUNING

A total of fourteen parameters of the second-order LPTN can be tuned using particle swarm optimization through the method described in [14]. This algorithm is a stochastic population-based approach where a collection of individuals (particles)—combinations of parameters to tune—are attracted to a best location with reference to a cost function value and the entire population, until a convergence criterion is achieved. Initial parameters can be approximated using the analytical formulas for heat transfer in electrical machines [23], [24]. Optimization boundaries are defined to avoid tuning values that have no physical sense. The optimization objective is to find the set of parameters $\mathbf{p}$ that minimizes the mean-squared error (MSE) between the measured (θ_r) and estimated ($\hat{\theta}_r$) rotor temperatures across n samples:

$$\text{MSE} = \frac{1}{n}\sum_{i=1}^{n} \varepsilon_{r,i}(\mathbf{p})^2 \tag{12}$$

where $\varepsilon_{r,i} = \theta_{r,i} - \hat{\theta}_{r,i}$. The average MSE is calculated considering data from the nine tuning tests.

A sampling period $T_s = 1\,\text{s}$ is selected to achieve numerical stability when discretizing, as expressed in (11), while also reproducing the thermal behavior of the machine in real time. A preliminary sensitivity analysis on a significantly smaller time step of 1 ms showed that the accuracy is comparable. However, a low-pass filter may be required at the input of the torque to average contributions that demand a bandwidth above 1 Hz. It is worth noting that in this case, no data filtering is applied because torque requests follow the temperature dynamics.

The optimization solver stopping criterion is set to a function tolerance of 0.05° C. The Parallel Optimization Toolbox is used to parallelize the work in sixteen instances of MATLAB R2025a to reduce the computational time. The identification process takes about 2 hours in a workstation equipped with an AMD Ryzen 9 3950X 16-core processor (3.49 GHz) and 64 GB of RAM. The identified values and its boundaries are listed in Table 2.

TABLE 2. LPTN parameters following the tuning procedure.

Parameter	Unit	Initial value	Lower bound	Upper bound	Optimal value
C_m	J/K	7213.5	5000	9000	7091.5
C_s		3381.7	2000	7000	6294.6
$R_{cs,0}$	K/W	0.0039	0.0005	0.1	0.0044
$R_{sr,0}$		0.2491	0.1	0.5	0.2234
$R_{wr,0}$		0.1013	0.01	1.5	0.0619
R_{sw}		0.0206	0.01	0.1	0.0343
$R_{ra,0}$		0.1459	0.1	0.3	0.1270
a_{sr}		0.2230	0.1	0.5	0.2612
a_{wr}		0.2536	0.1	0.5	0.2652
a_{ra}		0.0372	0.01	0.1	0.0271
b_{sr}	–	0.2258	0.1	0.5	0.1165
b_{wr}		0.5916	0.1	1	0.2793
b_{ra}		0.1123	0.05	0.3	0.1946
α_{cs}	1/K	-0.0012	-0.1	0	-0.0008

C. LPTN INITIAL CONDITIONS

The accuracy of the LPTN model is highly sensitive to the initial temperature conditions. This issue is more relevant in the estimation of the rotor/magnet temperature due to its large thermal time constant. Therefore, any deviation in the initial value will significantly increase the time the model takes to converge. Indeed, the initial temperature determination

has been scarcely discussed in the literature, where most of the works use the initial measured temperature equal to fixed initial conditions [6], [9], [14], [15], [28]. Nevertheless, a practical real-time implementation requires the knowledge of proper initial conditions to guarantee fast convergence and thus, minimal estimation error. Liang et al. recently proposed a method to determine the initial temperatures for real-time thermal models based on the temperature information of a sensor installed in the active winding or end winding [29]. On the other hand, [30] have used random initial conditions within an expected operating range to fit the parameters of the thermal network, thus making the model robust against variability.

The top of Fig. 7 shows a box plot of the coolant, winding, ambient, and rotor initial temperatures across the tuning and validation datasets. It is observed that the coolant and winding temperatures have a close median, interquartile range, minimum and maximum values. The reason is that measurement logs were captured starting with the electric motor turned off, while the cooling circuit was working for a sufficiently long period to achieve a thermal steady-state condition. Since conduction heat transfer is predominant between the winding and the stator, the coolant and winding temperatures result in similar values. On the other hand, the estimation of the rotor temperature requires a temperature with a lower median than the previous two, which can only be achieved with the ambient temperature. Therefore, the combination of the coolant and ambient temperatures is evaluated to find an optimal relationship using

$$\theta_{\mathrm{ic}} = \theta_{\mathrm{ic,a}}(1 - x_{\mathrm{f}}) + \theta_{\mathrm{ic,c}}\, x_{\mathrm{f}} \tag{13}$$

$$x_{\mathrm{f}} \in \{\mathbb{R} \mid 0 \leq x_{\mathrm{f}} \leq 1\} \tag{14}$$

where x_{f} is a fraction coefficient and the subindex ic refers to the initial condition. It should be noted that the winding temperature can be used instead of the coolant temperature due to the reasons discussed previously. Here, the coolant temperature was preferred since it is a sink temperature, as is the ambient temperature.

The middle plot in Fig. 7 depicts the mean-squared error of the initial rotor temperature—denoted MSE_1—as a function of the fraction coefficient x_{f} using (14) across all the datasets.

Results show that the minimal MSE, marked with a star in Fig. 7, is located at $x_{\mathrm{f}} = 0.46$ and MSE_1 equal to $10.05°\mathrm{C}^2$. Since the fraction coefficient is very close to the average condition ($x_{\mathrm{f}} = 0.5$), a simple average between the initial measured coolant and ambient temperatures is performed:

$$\theta_{\mathrm{r},1} = \frac{\theta_{\mathrm{c},1} + \theta_{\mathrm{a},1}}{2} \tag{15}$$

The outcomes from applying the initial condition in (15) are shown at the bottom of Fig. 7. The initial error in this condition has a mean absolute error of 2.4° C, a MSE_1 of $10.56°\mathrm{C}^2$, and a maximum value of 8.18° C.

Oppositely, if the rotor initial conditions are defined equal to the average ambient temperature, 20° C, which is a common assumption due to the large surface area of the rotor with the air, the performance is notably decreased. The initial error has a mean absolute value of 8.95° C, a MSE_1 of $130.82°\mathrm{C}^2$, and a maximum value of 21.43° C.

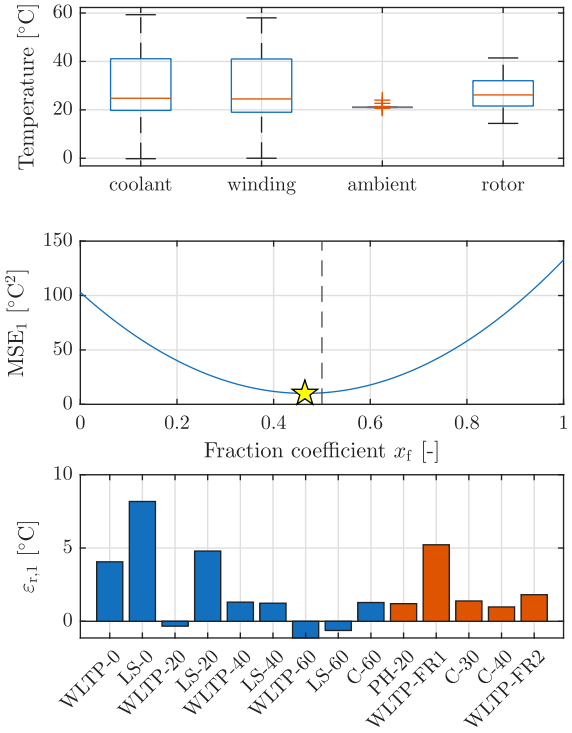

FIGURE 7. Rotor initial condition analysis. Box plot of initial temperature for the measured thermal nodes (top). Sensitivity analysis of the mean-squared error for the rotor initial condition as function of the fraction coefficient where the star marks the minimal value (middle). Temperature error for the rotor initial condition when $x_{\mathrm{f}} = 0.5$ for the fitting (blue) and validation (orange) datasets (bottom).

In contrast, the stator temperature tends to be similar to the winding temperature in steady state due to its proximity and the conduction heat transfer mechanism. Therefore, the initial measured winding temperature becomes the initial condition for the estimated stator temperature: $\theta_{\mathrm{s},1} = \theta_{\mathrm{w},1}$.

III. RESULTS

The performance of the model in both tuning and validation duty cycles is assessed using the instantaneous rotor temperature error ε_{r}. Performance metrics of mean-squared-error (MSE), root-mean-squared error (RMSE), mean absolute error (MAE), infinity norm error ($\|\varepsilon_{\mathrm{r}}\|_\infty$), and R-squared value ($\mathrm{R}^2$) were computed from the instantaneous error using:

$$\mathrm{MSE} = \frac{1}{n}\sum_{i=1}^{n} \varepsilon_{\mathrm{r},i}^2 \tag{16}$$

$$\mathrm{RMSE} = \sqrt{\frac{1}{n}\sum_{i=1}^{n} \varepsilon_{\mathrm{r},i}^2} \tag{17}$$

$$\mathrm{MAE} = \frac{1}{n}\sum_{i=1}^{n} |\varepsilon_{\mathrm{r},i}| \tag{18}$$

$$\|\varepsilon_r\|_\infty = \max_i |\varepsilon_{r,i}| \tag{19}$$

$$R^2 = 1 - \frac{\sum_{i=1}^{n}(\theta_{r,i} - \hat{\theta}_{r,i})^2}{\sum_{i=1}^{n}(\theta_{r,i} - \bar{\theta}_r)^2} \tag{20}$$

where n is the sample size and $\bar{\theta}_r$ is the mean of the rotor temperature measured values. In particular, the infinity norm error provides a measurement of the largest deviation between predicted and observed values, whereas the R-squared value quantifies the level of variation in the dependent variable that can be explained by the model.

Additionally, the normalized root-mean-squared error (NRMSE) is derived from the ratio of the RMSE and the observed standard deviation (σ_r), which makes it dimensionless. It produced the normalized difference between observed and predicted values given by

$$\text{NRMSE} = \frac{\text{RMSE}}{\sigma_r} = \frac{\sqrt{\sum_{i=1}^{n}\left(\varepsilon_{r,i} - \hat{\varepsilon}_{r,i}\right)^2}}{\sqrt{\sum_{i=1}^{n}\left(\varepsilon_{r,i} - \hat{\varepsilon}_r\right)^2}} \tag{21}$$

The previous metrics have been used extensively in the literature to evaluate the model performance [14], [19], [22], [31], [32]. Table 3 and Table 4 display the results for these metrics for the tuning and validation datasets, respectively.

Figures 8 and 9 show the measured temperature in the windings (top), measured and estimated rotor temperatures (middle), and instantaneous rotor temperature error (bottom) for the WLTP cycles and LS cycles from the tuning dataset, respectively.

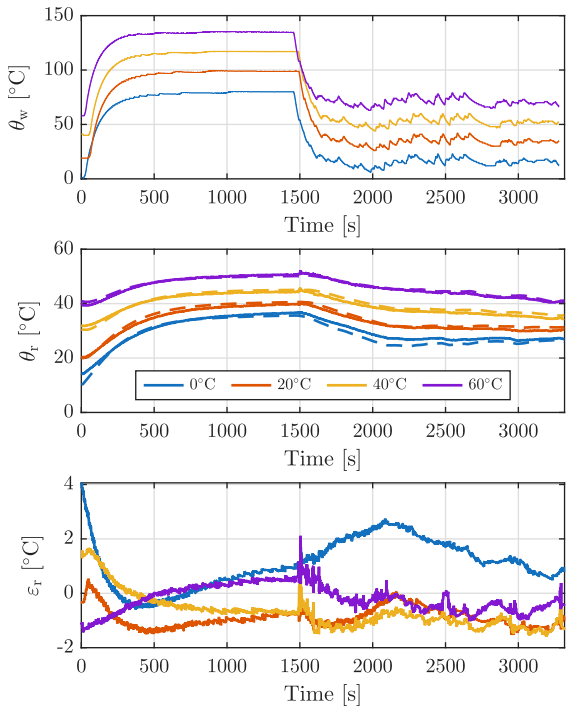

FIGURE 8. WLTP cycles for tuning at different inlet coolant temperatures. Winding temperature measurement (top), rotor temperature (middle), and rotor temperature error (bottom). For the rotor temperature, measured (solid) and estimate (dashed) are shown.

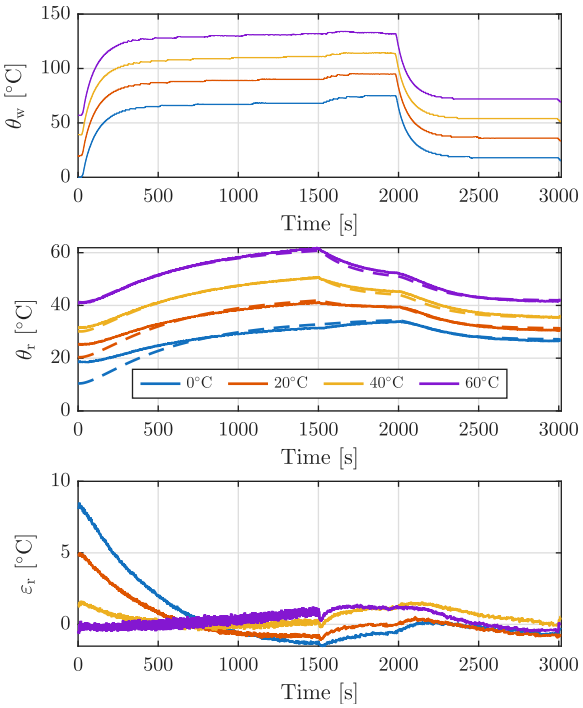

FIGURE 9. LS cycles for tuning at different inlet coolant temperatures. Winding temperature measurement (top), rotor temperature (middle), and rotor temperature error (bottom). For the rotor temperature, measured (solid) and estimate (dashed) are shown.

Figure 10 plots the same variables for the pulse-hold (PH) validation cycle at 20° C, which is the longest dataset.

Finally, WLTP validation dataset results appear in Fig. 11, while Fig. 12 illustrates the obtained behavior for the continuous working points, covering both the tuning and validation datasets.

In order to evaluate the performance in real-time hardware, a Processor-in-the-Loop (PIL) simulation was performed using MATLAB and a C2000™ LaunchPad with a TMS320F28069M microcontroller from Texas Instruments. The microcontroller features 90 MHz of operating frequency, 256 KB of flash memory and 100 KB of RAM. Results show an execution time of 19.7 [μs] and a CPU utilization of 0.002 [%].

IV. DISCUSSION

Table 3 shows that the MSE, RMSE, and MAE decrease with the increase of the inlet coolant temperature for the WLTP and LS cycles. This trend is clearly observed in Fig. 9, where the additional effect of a reduced error in the initial conditions with the increased inlet coolant temperature contributes to a favorable estimation performance. Moreover, the error in steady-state for all the inlet coolant temperatures is close to zero, which highlights a good convergence against diverse initial conditions, with a maximum estimation error of 8.5° C. The performance of the WLTP cycles (see Fig. 8) indicates a steady-state error within ±2° C. This value is shown to decrease with higher coolant temperatures. Nevertheless, the

TABLE 3. Performance metrics evaluated with the tuning dataset. Refer to Table 1 for details regarding the duty cycles.

Metric	WLTP-0	LS-0	WLTP-20	LS-20	WLTP-40	LS-40	WLTP-60	LS-60	C-60	Average
MSE	1.988	4.880	0.914	1.659	0.858	0.521	0.272*	0.423	0.453	1.330
RMSE	1.410	2.209	0.956	1.288	0.926	0.722	0.521*	0.651	0.673	1.040
MAE	1.185	1.302	0.893	0.806	0.849	0.549	0.436*	0.517	0.634	0.797
$\|\varepsilon_r\|_\infty$	4.073	8.512	1.528	5.039	1.679	1.640	2.111	1.386	1.357*	3.036
R^2	0.916	0.685	0.956	0.917	0.937	0.983	0.980	0.992*	0.845	0.912
NRMSE	0.290	0.561	0.210	0.288	0.251	0.132	0.143	0.091*	0.393	0.262

*Best value for each metric.

TABLE 4. Performance metrics evaluated with the validation dataset. Refer to Table 1 for details regarding the duty cycles.

Metric	PH-20	WLTP-FR1	C-30	C-40	WLTP-FR2	Average
MSE	0.533*	0.727	1.182	0.700	3.780	1.384
RMSE	0.730*	0.853	1.087	0.837	1.944	1.090
MAE	0.569	0.430*	1.027	0.768	1.880	0.935
$\|\varepsilon_r\|_\infty$	1.737	5.231	1.599	1.271*	2.502	2.468
R^2	0.924	0.958*	0.838	0.913	0.735	0.874
NRMSE	0.276	0.204*	0.403	0.296	0.515	0.339

*Best value for each metric.

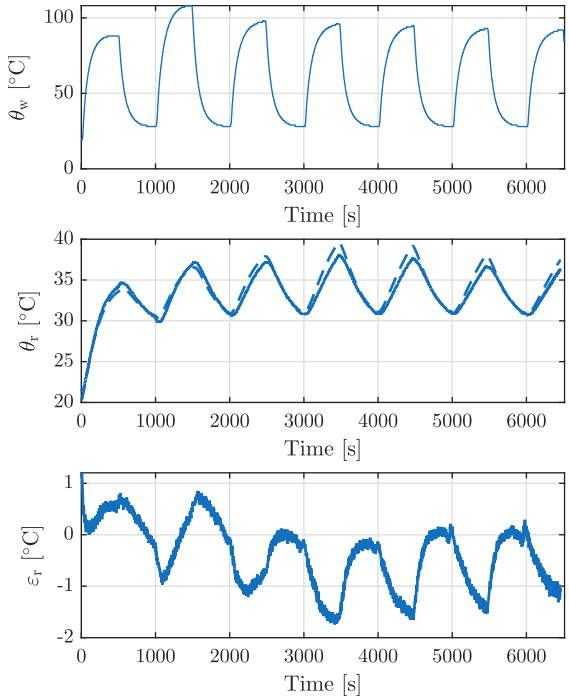

FIGURE 10. PH cycle for validation at an inlet coolant temperature of 20° C. Winding temperature measurement (top), rotor temperature (middle), and rotor temperature error (bottom). For the rotor temperature, measured (solid) and estimate (dashed) are shown.

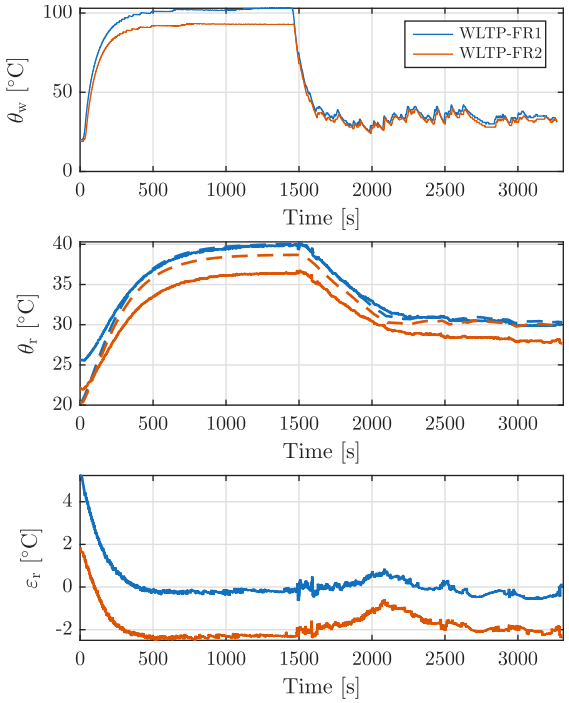

FIGURE 11. WLTP-FR1 and WLTP-FR2 cycles for validation. Winding temperature measurement (top), rotor temperature (middle), and rotor temperature error (bottom). For the rotor temperature, measured (solid) and estimate (dashed) are shown.

error in the initial condition has no correlation with the increasing coolant temperature, but the largest error is at the coldest inlet temperature.

Furthermore, Table 3 highlights R-squared values above 0.9 for most of the WLTP and LS driving cycles, except for the LS cycle at 0° C, due to the initial estimation error. This highlights the model robustness against different initial conditions. Although the flow rate is approximately 30% greater in the continuous working point dataset with the coolant at 60° C, the R-squared value is penalized minimally at 0.845.

Table 4 shows that the validation metrics for the MSE, RMSE, MAE, and NRMSE are within the range obtained in the tuning metrics of Table 3, which suggest a similar performance. The lowest error for the validation metrics is for the pulse-hold (PH-20) driving cycle, where the maximum error is contained within ±2° C, as shown in Fig. 10. On the other hand, the R-squared value is the largest for the WLTP-FR1 cycle, despite having the highest infinity norm error due to the inexact estimation of the initial conditions. The favorable fitting in the WLTP-FR1 cycle is due to its

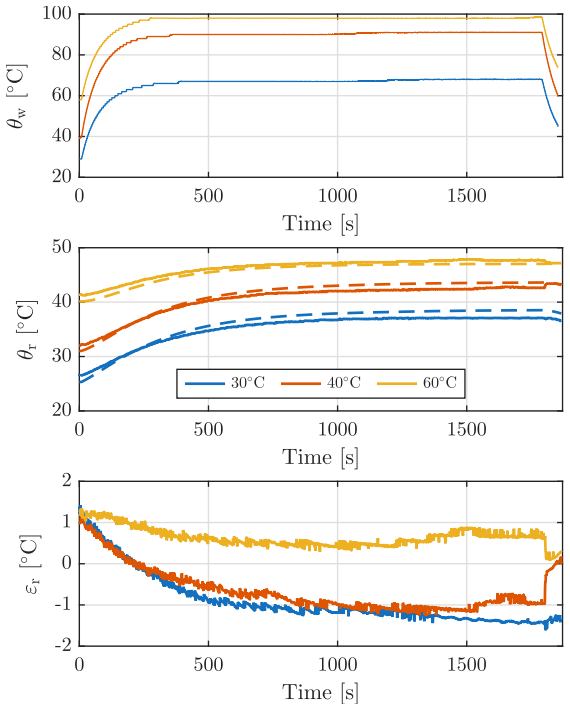

FIGURE 12. C cycles for tuning (60° C) and validation (30° C and 40° C). Winding temperature measurement (top), rotor temperature (middle), and rotor temperature error (bottom). For the rotor temperature, measured (solid) and estimate (dashed) are shown.

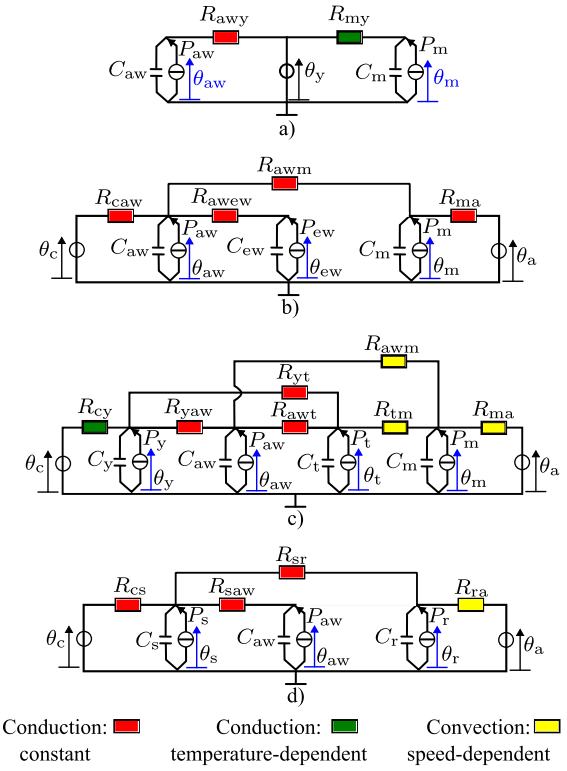

FIGURE 13. Comparison of reduced-order LPTNs present in the state-of-the-art: a) Second-order LPTN [15], b) Third-order LPTN [28], c) Fourth-order LPTN [14], and d) Third-order LPTN with LSTM [30].

close similarity with the WLTP-20 tuning dataset, but it differs in the initial conditions and the instantaneous average coolant temperature. Conversely, the poorest performance is obtained with the WLTP-FR2 cycle, most likely caused by a steady-state error close to 2° C. However, the $\|\varepsilon_r\|_\infty$ is contained within 2.5° C, which is acceptable for the intended application. This is a result of the identified model parameters, which represent an average behavior that is less precise at the extremes of the operating range. The WLTP-FR2 cycle has a high flow rate, 14.9 l/min, that is far from the average flow rate in the tuning datasets. A similar condition occurs in the C1-30 validation cycle, which has the second largest NRMSE and a flow rate of 14.9 l/min. An exception in this trend occurs in the continuous dataset C2-40, which exhibits a significantly better fitting than the previous two, although having a similar flow rate. A further discussion on this limitation and an alternative solution are presented in Section IV-B.

A. COMPARISON WITH THE STATE OF THE ART

The main distinguishing elements of this work and its contributions to the state-of-the-art are discussed subsequently. Kral et al. developed a second-order LPTN for an inner-rotor PMSM with a water cooling jacket for traction applications (Fig. 13-a) [15]. It consists of the permanent magnet and stator winding thermal nodes, and the stator core temperature as an input quantity to the model. Therefore, the stator iron losses are neglected. The total number of parameters is five, including those in the speed-dependent resistance between the magnet and the core. Results show a minimum and maximum RMSE values of 0.9° C and 3.4° C, respectively, for the estimation of the magnet temperature. Although this is one of the simplest models in the literature, it may not be valid for outer-rotor PMSM where the effect of air forced convection is more significant. Additionally, as pointed by [9] and [28], and verified from the identified parameter values of Table 2 ($R_{wr,0}$ and a_{wr}), the heat transfer between winding and rotor domains is not negligible, which can reduce the estimation accuracy of the model in [15]. Initial conditions adopted by Kral et al. are not discussed, but they are assumed equal to the initial measured temperature from the results.

Similarly, Huber et al. developed a third-order LPTN for an inner-rotor PMSM with varying coolant temperature (Fig. 13-b) [28]. The thermal nodes are the stator winding, end-winding and permanent magnet, while the inputs are the coolant and ambient temperatures. The stator iron losses and, consequently, the heat flow dissipated to the ambient and the rotor were neglected. Thus, the model may display deviations at high speeds where iron losses are more significant. The heat transfer from the end-winding to the rotor was also neglected, which may reduce model accuracy at peak operating conditions. The total number of parameters is eleven, including the terms to split the iron losses. However, they were identified as a set of non-varying terms in several regions within the operating region of the motor depending on

the applied current and speed. Results for the cross-validation show a maximum error within ±3° C considering different thermal excitation profiles, including ambient and coolant temperatures. Here again, the initial conditions are equal to the measured temperatures from the temperature profiles.

Later, Wallscheid and Bocker proposed a fourth-order LPTN for an inner rotor PMSM with a water cooling jacket for traction applications (Fig. 13-c) [14]. The thermal nodes are the stator yoke, stator teeth, stator winding and permanent magnets, and the temperature inputs are the coolant and the ambient. In total, 30 parameters are defined because the system is linear parameter-varying (LPV) due to the speed-dependent convection resistances connected to the magnet node and the temperature-dependent resistance between the stator yoke and the coolant. Results in cross-validation show a maximum estimation error of 8° C under complex load profiles with initial conditions equal to the measured temperatures. Due to its robustness, adaptability for real-time applications and accuracy suitable for automotive applications, the model has been the basis for recent works [6], [9], [30].

As motivated before, this work takes the work from Wallscheid and Bocker [14] as a basis, but contributes in reducing the uncertainty from the winding node, while exploiting the availability of winding temperature sensors in PMSM traction machines. For simplicity, the stator nodes are combined, which yields a total of fourteen parameters. Moreover, a focused definition of the initial conditions is proposed based on available measured temperatures. This has demonstrated to contribute in the reduction of the estimation error. Additionally, the method was validated in an outer-rotor PMSM with a cooling jacket for in-wheel traction, an application that has been rarely discussed in the literature.

Among the alternative LPTNs derived from the work in [14], the work by Liu et al. proposed a third-order LPTN, which includes a LSTM neural network at the output (Fig. 13-d) [30]. The thermal nodes of the LPTN are the stator yoke, stator winding and rotor, and the inputs are the coolant and ambient temperatures. The total number of parameters is 21, which are identified in a two-step procedure using ultra-low-speed and full-operating-condition datasets with random initial values within predefined upper and lower boundaries. Although there are similarities in the LPTN structure with this work, key differences emerge. First, the thermal resistance that connects the winding and rotor was neglected in [30]. It has been found, however, that this term is relevant when considering the heat transfer due to air convection from the winding to the rotor. Thereby, a speed-dependent resistance is necessary between the two domains. Second, the winding node is a system state in [30], thus the associated thermal capacitance and power source are included. Here, the winding temperature is exploited through a dedicated sensor available in typical traction machines. This, significantly reduces the uncertainty associated to this node and improves indirectly the accuracy related to the rotor node. Third, Liu et al. maintain the thermal resistance between the coolant and the stator as constant, since the water-cooling temperature was kept at 20° C. In this implementation, the dependence on the coolant temperature is included and evaluated in a wide range of temperatures (from 0° C to 60° C). Similarly, the sensitivity on the coolant flow rate is evaluated in the range between 10 and 15 l/min for the tuning and validation datasets.

Table 5 presents a comparative summary of the reduced-order LPTN state-of-the-art discussed above. Due to the differences in machine characteristics and dataset profiles, it serves only as a qualitative comparison of the model performance. Inputs include temperatures and power losses, while outputs refer to estimated temperatures, and size is the number of parameters in the model.

B. FLOW RATE SENSITIVITY

The effect of the coolant flow rate, or equivalently, the coolant velocity in the thermal resistance between the coolant and the stator has been highlighted in literature related to thermal models [9], [15] and heat convection problems in electrical machines [24], [33]. The water cooling jacket is the principal thermal management solution in electric machines [34], [35]. Moreover, varying the coolant flow rate is a very common thermal management control strategy in literature [36] and industry applications [37]. Interestingly, the inclusion of a flow-rate-dependent thermal resistance for LPTNs has not been implemented in literature. Assuming that the cooling flow rate range stays within a single flow regime— laminar or turbulent—the following expression can be modified to account for the dependence of the average heat transfer coefficient of the cooling jacket with respect the flow rate [24]:

$$R_{\mathrm{cs}} = R_{\mathrm{cs0}} \exp\left(-\frac{\dot{Q}_{\mathrm{c}}}{\dot{Q}_{\mathrm{c,max}}}\frac{1}{b_{\mathrm{c}}}\right) + a_{\mathrm{c}} \tag{22}$$

where $\dot{Q}_{\mathrm{c,max}}$ and $\dot{Q}_{\mathrm{c}}$ are the maximum and current coolant flow rates, respectively. R_{cs0}, b_{c}, and a_{c} are constants that are obtained though the LPTN parameter tuning process described in Section II-B. Since the flow rate and speed are related by the cross-sectional area, the fluid speed can be exchanged in (22) to comply with the available sensor.

In this work, the flow rate was not included to prevent adding a further signal to the model that may not be always available. However, in the context of this research, the inclusion of this measurement could potentially improve the estimation accuracy of the LPTN. This is because the validation datasets with the largest errors correspond to the C1-30 and the WLTP-FR2 cycles, which have an average flow rate close to 15 l/min, whereas the tuning datasets have an average flow rate of 10.6 l/min (except those with an inlet temperature of 0° C and the continuous working point). Therefore, the non-negligible flow rate difference of more than 4 l/min is likely causing a steady-state error close to 2° C.

TABLE 5. Comparison of LPTN models from the literature for the estimation of the rotor temperature.

Algorithm	MSE [°C^2]	$\|\varepsilon_r\|_\infty$ [°C]	Inputs	Outputs	Size
Second-order LPTN [15]	-	5.5 (magnet)	3	2	5
Third-order LPTN [28]	-	3 (magnet)	5	3	11
Fourth-order LPTN [14]	3.64	7.37	6	4	34
Fourth-order LPTN improved [9]	-	2.3 (magnet)	6	4	14
Fifth-order LPTN [6]	4.44	4.99	3	5	43
Third-order LPTN with LSTM [30]	10.6	8.79	5	3	20
Proposed method	1.38	2.46	5	2	15

Additionally, for the tuning datasets, the duty cycles with an inlet temperature of 0° C that have larger flow rates show the largest NRMSE. Similarly, the continuous working point C1-60 that has the highest flow rate among the tuning datasets shows the second largest NRMSE, although the MSE, RMSE, and MAE are relatively low compared with the other cycles.

V. CONCLUSION

This paper proposed a reduced-order lumped-parameter thermal network to estimate the temperature of the rotor on an outer-rotor permanent-magnet synchronous machine. The reduced-order model demonstrated a favorable predictive performance, achieving a satisfactory average root-mean-squared error of 1.09° C on the validation datasets. This level of accuracy is well-suited to ensure thermal safety and operational reliability of the machine in real-world scenarios. The model was fed with the winding temperature measurement, which is usually available from sensors located in the hotspots of electric machines for demanding applications, such as electric powertrain. Additionally, the definition of initial conditions from the available coolant and ambient temperatures performed satisfactorily, with a maximum error of 8.18° C and mean absolute error of 2.4° C. These conditions ensure a better temperature estimation when compared with initial conditions at a fixed temperature. Moreover, the assessment was performed over multiple tuning and validation experimental data, where the machine was tested under a wide range of inlet coolant temperatures, flow rates, and duty cycles. Furthermore, the PIL results demonstrated the real-time feasibility of the thermal network. The effect of the flow rate on the accuracy of the estimate has been discussed, and an alternative formulation for thermal resistance that connects the coolant to the stator has been proposed to improve system accuracy in future work.

ACKNOWLEDGMENT

The authors would like to thank Elaphe Propulsion Technologies Ltd., in particular to Danylo Trinchuk and Matej Ocvirk, for providing the experimental data used in the development of the models and technical support.

REFERENCES

[1] I. Husain, B. Ozpineci, M. S. Islam, E. Gurpinar, G.-J. Su, W. Yu, S. Chowdhury, L. Xue, D. Rahman, and R. Sahu, "Electric drive technology trends, challenges, and opportunities for future electric vehicles," in *Proc. IEEE*, Jun. 2021, vol. 109, no. 6, pp. 1039–1059.

[2] S. Li, B. Sarlioglu, S. Jurkovic, N. R. Patel, and P. Savagian, "Analysis of temperature effects on performance of interior permanent magnet machines for high variable temperature applications," *IEEE Trans. Ind. Appl.*, vol. 53, no. 5, pp. 4923–4933, Sep. 2017.

[3] O. Wallscheid, "Thermal monitoring of electric motors: State-of-the-art review and future challenges," *IEEE Open J. Ind. Appl.*, vol. 2, pp. 204–223, 2021.

[4] X. Liao, S. Chen, Y. Long, and S. Zhao, "Neural dynamics model for temperature estimation of permanent magnet synchronous motor," *IEEE Trans. Veh. Technol.*, vol. 74, no. 8, pp. 11993–12003, Aug. 2025.

[5] Z. Ullah and J. Hur, "A comprehensive review of winding short circuit fault and irreversible demagnetization fault detection in PM type machines," *Energies*, vol. 11, no. 12, p. 3309, Nov. 2018.

[6] L. Cao, X. Fan, D. Li, W. Kong, R. Qu, and Z. Liu, "Improved LPTN-based online temperature prediction of permanent magnet machines by global parameter identification," *IEEE Trans. Ind. Electron.*, vol. 70, no. 9, pp. 8830–8841, Sep. 2023.

[7] D. Fernandez, D. Reigosa, T. Tanimoto, T. Kato, and F. Briz, "Wireless permanent magnet temperature & field distribution measurement system for IPMSMs," in *Proc. IEEE Energy Convers. Congr. Expo. (ECCE)*, Sep. 2015, pp. 3996–4003.

[8] S. Stipetic, M. Kovacic, Z. Hanic, and M. Vrazic, "Measurement of excitation winding temperature on synchronous generator in rotation using infrared thermography," *IEEE Trans. Ind. Electron.*, vol. 59, no. 5, pp. 2288–2298, May 2012.

[9] J. Feng, D. Liang, Z. Q. Zhu, S. Guo, Y. Li, and A. Zhao, "Improved low-order thermal model for critical temperature estimation of PMSM," *IEEE Trans. Energy Convers.*, vol. 37, no. 1, pp. 413–423, Mar. 2022.

[10] A. Acquaviva, O. Wallmark, E. A. Grunditz, S. T. Lundmark, and T. Thiringer, "Computationally efficient modeling of electrical machines with cooling jacket," *IEEE Trans. Transport. Electrific.*, vol. 5, no. 3, pp. 618–629, Sep. 2019.

[11] D. D. Reigosa, F. Briz, P. García, J. M. Guerrero, and M. W. Degner, "Magnet temperature estimation in surface PM machines using high-frequency signal injection," *IEEE Trans. Ind. Appl.*, vol. 46, no. 4, pp. 1468–1475, Jul. 2010.

[12] O. Wallscheid, A. Specht, and J. Böcker, "Observing the permanent-magnet temperature of synchronous motors based on electrical fundamental wave model quantities," *IEEE Trans. Ind. Electron.*, vol. 64, no. 5, pp. 3921–3929, May 2017.

[13] D. E. G. Erazo, O. Wallscheid, and J. Böcker, "Improved fusion of permanent magnet temperature estimation techniques for synchronous motors using a Kalman filter," *IEEE Trans. Ind. Electron.*, vol. 67, no. 3, pp. 1708–1717, Mar. 2020.

[14] O. Wallscheid and J. Böcker, "Global identification of a low-order lumped-parameter thermal network for permanent magnet synchronous motors," *IEEE Trans. Energy Convers.*, vol. 31, no. 1, pp. 354–365, Mar. 2016.

[15] C. Kral, A. Haumer, and S. B. Lee, "A practical thermal model for the estimation of permanent magnet and stator winding temperatures," *IEEE Trans. Power Electron.*, vol. 29, no. 1, pp. 455–464, Jan. 2014.

[16] O. Wallscheid, W. Kirchgässner, and J. Böcker, "Investigation of long short-term memory networks to temperature prediction for permanent magnet synchronous motors," in *Proc. Int. Joint Conf. Neural Netw. (IJCNN)*, May 2017, pp. 1940–1947.

[17] L. He, Y. Feng, Z. Yan, and M. Cai, "Rotor temperature prediction of PMSM based on LSTM neural networks," *Arabian J. Sci. Eng.*, vol. 49, no. 12, pp. 16685–16696, Dec. 2024.

[18] W. Kirchgässner, O. Wallscheid, and J. Böcker, "Deep residual convolutional and recurrent neural networks for temperature estimation in permanent magnet synchronous motors," in *Proc. IEEE Int. Electr. Mach. Drives Conf. (IEMDC)*, May 2019, pp. 1439–1446.
[19] J. Lee and J.-I. Ha, "Temperature estimation of PMSM using a difference-estimating feedforward neural network," *IEEE Access*, vol. 8, pp. 130855–130865, 2020.
[20] W. Kirchgässner, O. Wallscheid, and J. Böcker, "Estimating electric motor temperatures with deep residual machine learning," *IEEE Trans. Power Electron.*, vol. 36, no. 7, pp. 7480–7488, Jul. 2021.
[21] O. Wallscheid, T. Huber, W. Peters, and J. Böcker, "A critical review of techniques to determine the magnet temperature of permanent magnet synchronous motors under real-time conditions," *EPE J.*, vol. 26, no. 1, pp. 11–20, Jan. 2016.
[22] E. A. Martinez-Ríos, I. S. Aguilar-Zamorate, S. Pakštys, R. Galluzzi, and N. Amati, "Estimating temperature in a permanent-magnet synchronous motor using Hammerstein and nonlinear autoregressive models initialized via thermal networks," *IEEE Trans. Ind. Appl.*, early access, Aug. 4, 2025, doi: 10.1109/TIA.2025.3595135.
[23] D. A. Howey, P. R. N. Childs, and A. S. Holmes, "Air-gap convection in rotating electrical machines," *IEEE Trans. Ind. Electron.*, vol. 59, no. 3, pp. 1367–1375, Mar. 2012.
[24] D. A. Staton and A. Cavagnino, "Convection heat transfer and flow calculations suitable for electric machines thermal models," *IEEE Trans. Ind. Electron.*, vol. 55, no. 10, pp. 3509–3516, Oct. 2008.
[25] G. Bertotti, "General properties of power losses in soft ferromagnetic materials," *IEEE Trans. Magn.*, vol. 24, no. 1, pp. 621–630, Jan. 1988.
[26] P. Zhang, G. Y. Sizov, J. He, D. M. Ionel, and N. A. O. Demerdash, "Calculation of magnet losses in concentrated-winding permanent-magnet synchronous machines using a computationally efficient finite-element method," *IEEE Trans. Ind. Appl.*, vol. 49, no. 6, pp. 2524–2532, Nov. 2013.
[27] J. Böcker, "Discrete-time model of an induction motor," *Eur. Trans. Electr. Power*, vol. 1, no. 2, pp. 65–71, Mar. 1991.
[28] T. Huber, W. Peters, and J. Böcker, "A low-order thermal model for monitoring critical temperatures in permanent magnet synchronous motors," in *Proc. 7th IET Int. Conf. Power Electron., Mach. Drives (PEMD)*, Apr. 2014, pp. 1–6.
[29] D. Liang, Z. Q. Zhu, J. Feng, Y. Li, and S. Guo, "Initial temperature determination for real-time thermal models in permanent magnet synchronous machines," *IEEE Trans. Transport. Electrific.*, vol. 11, no. 1, pp. 2204–2218, Feb. 2025.
[30] Z. Liu, W. Kong, X. Fan, Z. Li, K. Peng, and R. Qu, "Hybrid thermal modeling with LPTN-informed neural network for multinode temperature estimation in PMSM," *IEEE Trans. Power Electron.*, vol. 39, no. 9, pp. 1–12, Sep. 2024.
[31] W. Kirchgässner, O. Wallscheid, and J. Böcker, "Thermal neural networks: Lumped-parameter thermal modeling with state-space machine learning," *Eng. Appl. Artif. Intell.*, vol. 117, Jan. 2023, Art. no. 105537.
[32] H. Jing, Z. Chen, X. Wang, X. Wang, L. Ge, G. Fang, and D. Xiao, "Gradient boosting decision tree for rotor temperature estimation in permanent magnet synchronous motors," *IEEE Trans. Power Electron.*, vol. 38, no. 9, pp. 10617–10622, Sep. 2023.
[33] D. Staton, A. Boglietti, and A. Cavagnino, "Solving the more difficult aspects of electric motor thermal analysis in small and medium size industrial induction motors," *IEEE Trans. Energy Convers.*, vol. 20, no. 3, pp. 620–628, Sep. 2005.
[34] P.-O. Gronwald and T. A. Kern, "Traction motor cooling systems: A literature review and comparative study," *IEEE Trans. Transport. Electrific.*, vol. 7, no. 4, pp. 2892–2913, Dec. 2021.
[35] X. Wang, B. Li, D. Gerada, K. Huang, I. Stone, S. Worrall, and Y. Yan, "A critical review on thermal management technologies for motors in electric cars," *Appl. Thermal Eng.*, vol. 201, Jan. 2022, Art. no. 117758.
[36] G. Previati, G. Mastinu, and M. Gobbi, "Thermal management of electrified vehicles—A review," *Energies*, vol. 15, no. 4, p. 1326, Feb. 2022.
[37] Y. Yamagishi, R. Idoguchi, H. Hirano, and T. Kawamura, "Cooling system for electric motor of vehicle," U.S. Patent 7 156 195 B2, Mar. 3, 2003.

IRVING S. AGUILAR-ZAMORATE received the B.Sc. degree in mechanical engineering and the M.S. degree in engineering science from the Tecnológico de Monterrey, Mexico City, in 2020 and 2022, respectively, where he is currently pursuing the Ph.D. degree in engineering science. His research stay at the Mechatronics Laboratory, Politecnico di Torino. His research interests include thermal management, temperature estimation, design, and control of electric machines for automotive and micro-mobility applications.

RENATO GALLUZZI (Senior Member, IEEE) received the M.Sc. and Ph.D. degrees in mechatronics from the Politecnico di Torino, Italy, in 2010 and 2014, respectively. Since 2011, he has been an Active Collaborator of the Mechatronics Laboratory at the Politecnico di Torino. He is currently a Research Professor with the School of Engineering and Sciences, Tecnológico de Monterrey, Mexico. He is the author of numerous journal publications and conference papers. He also holds inventorship in multiple international patents. His research interests include vibration control and damping systems, power actuators, electric machinery, and energy harvesting. He is a member of the National Research Fellows System Level 1 (SNII-1), SECIHTI, Mexico.

SAULIUS PAKŠTYS received the B.Sc. and M.Sc. degrees in mechanical engineering from the Politecnico di Torino, Turin, Italy, in 2021 and 2022, respectively, where he is currently pursuing the Ph.D. degree in mechanical engineering with the Mechatronics Laboratory. His research interests include energy management strategies for hybrid energy storage systems, alternative automotive powertrains, highly integrated battery systems design and their thermal management, and electric machine thermal analysis.

ERICK AXEL MARTINEZ-RÍOS was born in Mexico City, Mexico, in May 1995. He received the B.Sc. degree (Hons.) in mechatronics engineering and the M.Sc. degree (Hons.) in engineering science from the Tecnológico de Monterrey, Mexico City, in 2017 and 2022, respectively, where he is currently pursuing the Ph.D. degree in engineering science. From 2018 to 2020, he was a Project Specialist at the Tecnológico de Monterrey. He is the author of fourteen journal articles, four conference papers, and one book chapter. His research interests include signal processing, machine learning, and control theory.

NICOLA AMATI received the Ph.D. degree in machine design from the Department of Mechanical Engineering, Politecnico di Torino, Turin, Italy, in 2001. He joined the Politecnico di Torino, in 2001, as a Faculty Member, where he is currently a Full Professor with the Mechanical and Aerospace Engineering Department. He is also a Principal Investigator with the Center of Automotive Research and Sustainable Mobility, Politecnico di Torino. His research and lecturing interests focus on the analysis, design, and control of electromechanical systems, with an emphasis on rotating machinery, active and passive magnetic bearings and dampers, and more-electric systems for automotive applications.